ARTICLES

Deuteron threshold electrodisintegration at high momentum transfer

W. M. Schmitt, W. Turchinetz, C. F. Williamson, T. C. Yates,* and J. D. Zumbro†
Bates Linear Accelerator Center and Department of Physics, Massachusetts Institute of Technology, Cambridge, Massachusetts 02139

K. S. Lee,‡ H. Baghaei,§ S. Churchwell, R. S. Hicks, R. Miskimen, G. A. Peterson, and K. Wang‖
Department of Physics, University of Massachusetts, Amherst, Massachusetts 01003

P. E. Bosted and M. Spengos¶
Department of Physics, American University, Washington, D.C. 20016

B. Frois, J. Martino, and S. Platchkov
DPNHE, CEN Saclay, F-91191 Gif-sur-Yvette, France

A. Hotta
Department of Physics, Shizuoka University, Shizuoka 422, Japan
(Received 9 April 1997)

Absolute differential cross sections for the threshold electrodisintegration of the deuteron with good resolution were measured at a laboratory scattering angle of 160° for five values of Q^2 ranging from 8.66 to 42.4 fm^{-2}. Comparisons of the data averaged over E_{np} from 0 to 3 MeV and from 0 to10 MeV are made with nonrelativistic meson exchange calculations. These calculations are sensitive to the nucleon electromagnetic form factors, nucleon-nucleon potential, and relativistic effects. The data are also compared with a hybrid quark-hadron model calculation that describes the deuteron as a six-quark cluster for the short range part of the interaction. Some of these calculations can describe the data reasonably well over certain ranges of Q^2; however, none of these calculations can accurately describe the data over the entire measured Q^2 range. [S0556-2813(97)01510-0]

PACS number(s): 25.30.Dh, 24.10.−i, 25.10.+s, 27.10.+h

I. INTRODUCTION

The bound two-nucleon system, the deuteron, has for more than half a century been under intensive experimental and theoretical investigation. It is the simplest nuclear system and as such is an essential subject for the study of nucleon-nucleon interactions.

The ground state of the deuteron is the only bound state of the two-nucleon system. It is a spin triplet state with $J^\pi = 1^+$ and isospin $T=0$. It is dominantly a $^3S_1$ configuration with a 4–7% admixture of $^3D_1$. The latter admixture gives rise to the nonzero quadrupole moment of the deuteron and provides experimental proof for tensor components in the nucleon-nucleon interaction. The deuteron ground state is very weakly bound by only about 2.22 MeV.

The first excited state of the deuteron is unbound by only a few hundred keV. This is a spin singlet 0^+ state of configuration $^1S_0$ and is the $T_z=0$ member of the $T=1$ isospin triplet of the two-nucleon system. Excitation of this state is by an $M1$ isovector spin-flip transition from the ground state. This state manifests itself in, for example, electrodisintegration experiments where there is observed a prominent resonant feature in the reaction strength just above the breakup excitation energy. The first 3 or so MeV above breakup threshold is observed to be predominantly of $M1$, $\Delta T=1$ character as one would expect, since this is the only resonant channel in this range of excitation energy.

The character of this transition, $M1$ isovector spin flip, suggests that the breakup of the deuteron in the first few MeV above threshold may contain significant contributions from meson exchange currents and isobar configurations. The possibility that deuteron breakup near threshold might serve as a laboratory for studying subnucleon degrees of freedom in nucleon-nucleon interactions has long motivated both experimental and theoretical activity. The electromagnetic interaction provides an almost ideal probe for these types of studies since the interaction is known, allowing one to focus clearly on the nuclear structure aspects of the problem. Inelastic electron scattering is particularly useful since it allows one to maintain a constant energy transfer while varying the momentum transfer. To first order, this maps the

*Present address: Andersen Consulting, Columbus, OH 43215.
†Present address: Mail Stop H846, Los Alamos National Laboratory, Los Alamos, NM 87545.
‡Present address: Korea University, Seoul, Korea, 136-701.
§Present address: University of Texas M.D. Anderson Cancer Center, Houston, TX 77030.
‖Present address: University of Virginia, Charlottesville, VA 22901.
¶Present address: Deutsches Electronen-Synchrotron DESY, Hamburg, Germany.

Fourier transform of the spatial distribution of the transition current between the ground state and the continuum state. It is this transition current that is calculated from the various theoretical models of the two-nucleon system.

A. Previous work

Experimental interest in the threshold electrodisintegration of the deuteron dates to the early days of electron scattering [1–4]. In terms of the four-momentum transfer Q_μ, these early experiments were carried out for $Q^2 \leqslant 10$ fm^{-2}. They were compared to an impulse approximation calculation of Jankus [5] that included only the $^3S_1$ component in the ground state and no meson exchange currents. It was clear even at these very low momentum transfers that the observed threshold electrodisintegration strength for most of the experiments was significantly larger than predicted by this theory.

Later calculations [6–9] made more complete by including a $^3D_1$ component in the ground state, some meson exchange currents, and isobar currents showed good agreement with the experimental data for threshold electrodisintegration in the range $Q^2 \leqslant 10$ fm^{-2}. These results also showed most dramatically that the one-body currents produced a deep interference minimum at $Q^2 \approx 12$ fm^{-2} and that almost the entire strength in that region is dominated by two-body exchange currents. For higher momentum transfers these calculations also predicted a sensitive cancellation between the one-body and two-body amplitudes and in this kinematic region there were strongly differing predictions by the various calculations.

These experimental and theoretical results clearly indicated that threshold electrodisintegration of the deuteron could serve as a sensitive test of models of meson exchange currents. The experimental data were extended up to $Q^2 = 19$ fm^{-2} by Bernheim *et al.* [10] and up to $Q^2 = 28$ fm^{-2} by Auffret *et al.* [11]. These experiments extended the data set through the region of the minimum in the one-body amplitude at about 12 fm^{-2} where the meson exchange and isobar currents were expected to dominate. These data prompted a number of new theoretical calculations based on potential models [12–19] and on hybrid quark-hadron models [20–22]. Fits to the experimental data ranged from fair to good for the various models; however, it was clear that the experimental data stopped at a momentum transfer just below that at which there was a large divergence in the predictions of the various calculations.

The present high-resolution experiment achieved Q^2 values in the sensitive kinematic region above 40 fm^{-2}. A preliminary summary of the results of this experiment has been reported previously [23]. This paper will present a more complete discussion of the data analysis along with a detailed description of the experimental details for the measurement. A similar experiment covering a wider range of momentum transfer but with much poorer resolution has been carried out at SLAC [24,25].

B. Kinematics

Figure 1 shows the Feynman diagram for the electrodisintegration reaction in the one-photon exchange approximation in which P_e and P_e' are the laboratory four-momenta for

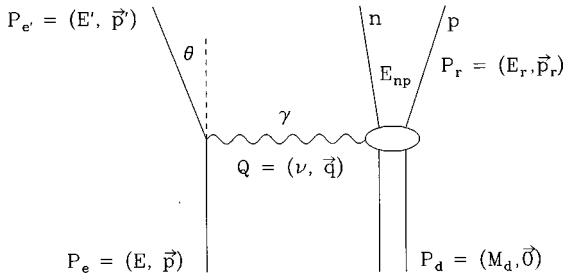

FIG. 1. The electrodisintegration reaction in the one-photon exchange approximation.

the incident and scattered electron, P_t that of the target deuteron, and P_r that of the recoil neutron-proton system. Neglecting the rest mass of the electron, the square of the four-momentum transfer is defined as

$$Q^2 = -Q_\mu^2 = 4EE' \sin^2(\theta/2). \tag{1}$$

The excitation energy of the recoiling deuteron is defined as the difference between the invariant masses, $E_{\rm ex} = M_d^* - M_d$, where $(M_d^*)^2 = P_r^2$ and $(M_d)^2 = P_d^2$ with M_d being the rest mass of the deuteron. For excitation energies greater than the deuteron binding energy of 2.22 MeV, the deuteron breaks apart. It is useful for the electrodisintegration reaction to define the quantity $E_{np} = E_{\rm ex} - 2.22$ MeV, which is the relative kinetic energy of separation of the neutron-proton system, and just at breakup $E_{np} = 0$.

II. EXPERIMENTAL APPARATUS AND PROCEDURE

Because existing theoretical calculations indicated that the threshold cross sections could be as small as 10^{-40} cm^2 sr^{-1} MeV^{-1} at the highest Q^2 point, considerable effort was devoted to maximizing the luminosity while minimizing the various sources of background. A liquid deuterium target was used in order to maximize the number of nuclei per cm^2. Good resolution [<1.5 MeV full width at half maximum (FWHM)] was also required to separate the elastic peak from the breakup threshold (2.22 MeV). The scattered electrons were momentum analyzed by the ELSSY dispersion matched spectrometer which has an intrinsic momentum resolution $\delta p/p$ less than 10^{-4}. The ELSSY detector system was upgraded with new horizontal drift chambers to restrict the angular acceptance of cosmic ray events, a lead glass detector array to distinguish high-energy cosmic ray muons from electrons, and a gas Čerenkov detector for π^- discrimination.

A. Electron beam

This experiment was performed at the MIT-Bates Linear Accelerator Center. The beam could be recirculated to provide electron energies ranging from 347 to 913 MeV. The average beam current used in this experiment was 25 μA with a 1% duty factor and with an intrinsic energy spread of 0.3%. At all but the highest bombarding energies the maximum usable beam current was limited by the cooling capacity of the target cryogenic refrigerator.

The position of the beam spot on the target was monitored by two sets of secondary emission monitors, one set horizon-

tal and one set vertical. These defined a rectangular area through which essentially all of the beam should pass. Wandering of the beam generated a signal in one or more of these monitors which inhibited data acquisition until the beam was properly recentered. Beam halo was monitored by plastic Cerenkov detectors mounted near the beam pipe upstream from the target. The beam was tuned to minimize the signal in these detectors.

The energy calibration of the beam had been carried out previously only for energies up to 500 MeV [26]. The calibration for higher energies was based on an extrapolation of the calibration at lower energies. However, at the highest bombarding energy, elastic scattering from liquid hydrogen was also measured which helped to constrain the energy uncertainty at the furthest point in the extrapolation. The overall uncertainty in the energy calibration was estimated to be about 1%. Since the deuterium elastic peak was not expected to be clearly visible at the highest bombarding energies due to the extremely small size of the cross sections, data were also taken for the reaction $^2\mathrm{H}(e^-,\pi^-)$ at the kinematic end point. This reaction had a much larger count rate and allowed a more accurate positioning of the deuterium elastic peak on the spectrometer focal plane by scaling the spectrometer magnets relative to the pion end point than the bombarding energy uncertainties could give alone.

The total charge for a run was measured by sending a signal from a nonintercepting toroidal transformer to a precision charge integrator. This system was calibrated by sending a signal from a precision pulser into a winding that simulated the beam [27]. The absolute accuracy of integration was of the order of 0.1%.

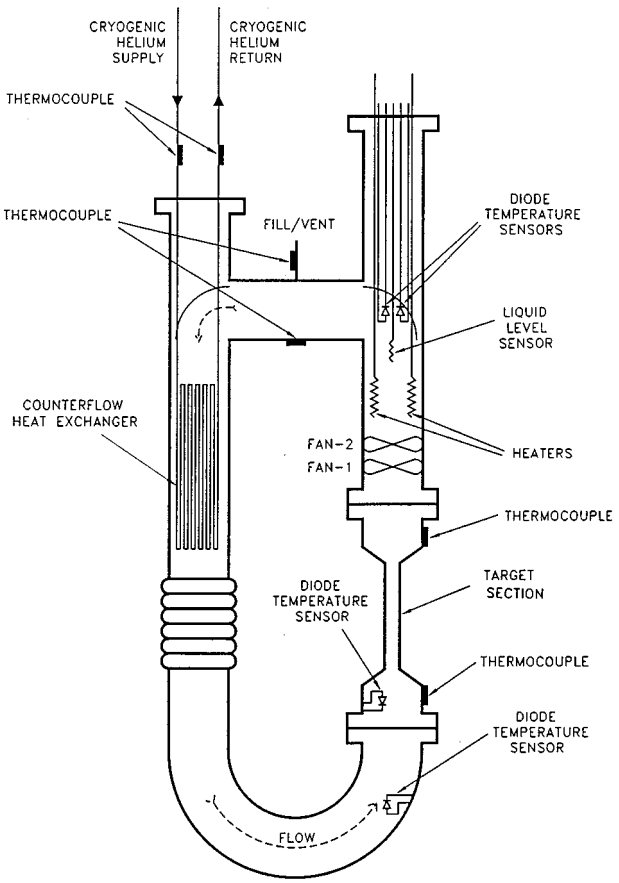

FIG. 2. A schematic diagram of the Bates liquid deuterium target loop.

B. Liquid deuterium target system

The Bates high-power liquid target system was used in this experiment. This system is capable of producing either a liquid deuterium or a liquid hydrogen target, and targets of both isotopes were used in this experiment. The design, operation, and safety of the system is discussed in detail elsewhere [28,29], and so only a brief description will be given here.

The liquid deuterium target system consisted of three main parts: a 200 W cryogenic helium refrigerator, a target loop, and a gas handling valve panel. The refrigerator supplied cryogenic helium to a counterflow heat exchanger located inside the target loop. The gas handling valve panel contained the necessary plumbing to direct the flow of the target gas from either a 12 400 ℓ reservoir or from high-pressure bottles into the target loop.

A schematic diagram of the target loop is shown in Fig. 2, which illustrates some of its features. The entire target loop is roughly 1 m in overall height, 0.5 m in width, and contained about 10 ℓ of liquid when full. The liquid was circulated in the loop by two immersed vaneaxial fans to speeds of the order of 2 m/s. The heat load on the system could be varied by means of immersed heaters, and the heater currents could be modulated by a signal derived from a beam current transducer in order to maintain a constant heat load on the target. The target loop was also equipped with several temperature and pressure sensors. These consisted of diode and thermocouple temperature sensors, mechanical pressure gauges, and precision electrical pressure transducers. These were monitored during the experiment for safety considerations and for accurate liquid density information. The readings from the various sensors were also written to magnetic tape as part of the data acquisition stream.

The target loop was mounted inside the scattering chamber assembly with feedthroughs at the top for cryogenic helium and gaseous deuterium. The electron beam passed perpendicularly through the narrow part of the target loop labeled in Fig. 2 as the target section. A horizontal section at beam height of this narrow part is shown in Fig. 3 along with the target collimating slits. The target section was fabricated by partial flattening of an aluminum pipe to reduce the amount of liquid traversed after scattering. This yielded a target about 10 cm in length and 3 cm in width with a wall thickness of 0.1 cm and was approximately elliptical in cross section. The target collimating slits were attached to a metal strut mounted from the top of the scattering chamber in order to isolate them thermally from the cold target loop. These slits were made from a machineable tungsten alloy of thickness 20 radiation lengths along the direction of the scattered electron. The purpose of these slits was to block the electrons which scatter from the aluminum entrance and exit end caps of the target section from the acceptance cone of the ELSSY spectrometer. These slits also defined the usable target length and were accurately positioned using a theodolite aligned on the optical axis of the ELSSY spectrometer. This yielded an effective liquid target length of 3.69 cm.

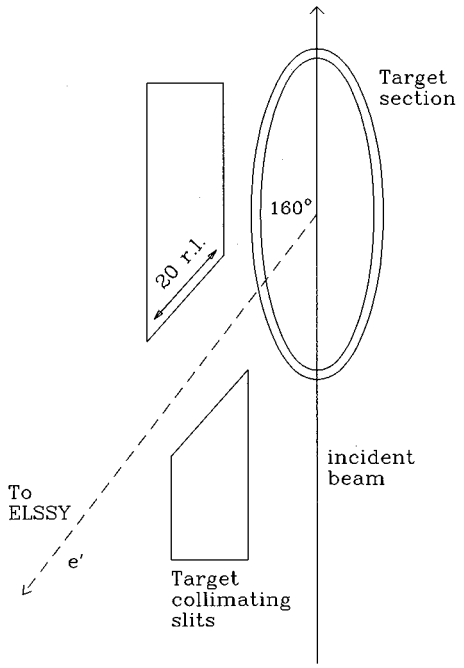

FIG. 3. A cross sectional view of the target section and target collimating slits.

C. ELSSY spectrometer system

The Bates ELSSY magnetic spectrometer is a high-resolution, dispersion matched system of dipole-dipole configuration [30] whose deflection angle is 90°, and whose dispersion along the focal surface is about 10 cm/%. Charged particles are deflected vertically downward into a semicircular pit; this geometry provides earthen shielding from background generated at the target. Its vacuum system is integral with the target chamber, so that scattered electrons do not traverse an entrance window, and only exit to the detectors through a thin composite vacuum window. The solid angle is determined by two pairs of tungsten alloy slits, one opening vertically and the other opening horizontally. These slits, located about 2 m from the target at the spectrometer entrance, were adjusted to give a maximum solid angle of 3.66 msr. The spectrometer was operated at a fixed angle of 160°.

A schematic diagram of the ELSSY detector system is given in Fig. 4. This system consisted of a vertical drift chamber (VDC), two horizontal drift chambers (HDC's), a dual plastic scintillator trigger detector, a gas Čerenkov detector, and an array of 14 lead-glass Čerenkov detectors. The VDC and HDC's were tilted at an angle of 45° with respect to horizontal to correspond approximately with the ELSSY focal surface. The location of the VDC was chosen to lie nominally along this focal surface which is located just outside the spectrometer exit flange, and is illustrated in the figure by the dashed line.

The VDC measured the focal plane position x_f and angle θ_f of a given electron trajectory in the dispersion plane. The intersection of the trajectory and the plane of the VDC could be measured with an accuracy better than ± 0.3 mm, and the angle could be measured to an accuracy of about ± 15 mr. The design, operation, and analysis of the VDC are discussed at length elsewhere [31,32].

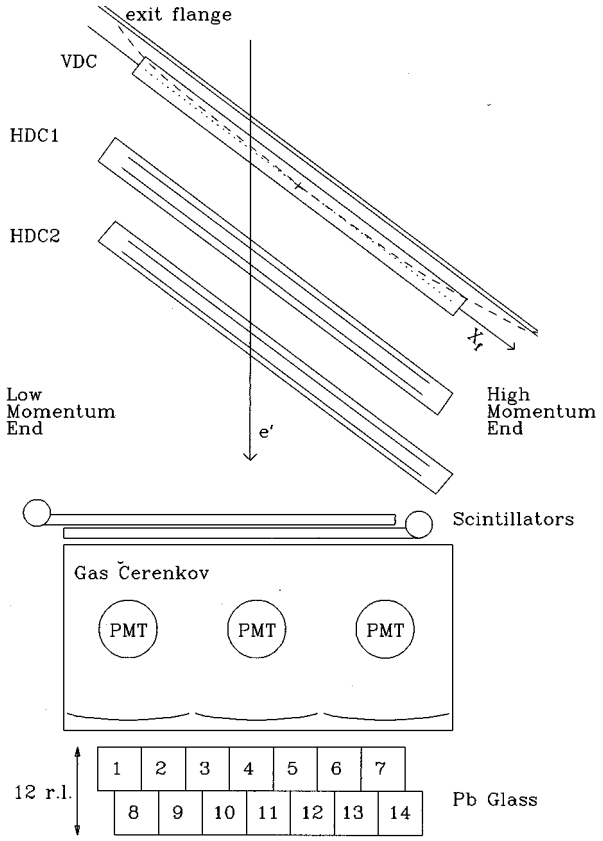

FIG. 4. The ELSSY detection system. The dashed curve illustrates the approximate location of the focal surface and coincides roughly with the position of the vertical drift chamber (VDC).

The HDC's allowed accurate measurement of the position y_f and angle ϕ_f of a trajectory in the plane perpendicular to the dispersion plane. The positional resolution was better than ± 0.3 mm and the angular resolution was of the order of ± 1 mr. Since the optics of ELSSY were designed to produce parallel rays from the target in this plane ($\phi_f \approx 0$), all cosmic rays except those in a narrow ϕ_f acceptance about the zenith were rejected in the analysis. These chambers are described in detail by Lee [33].

Reconstruction of the target z position had a resolution of the order of ± 3 cm. This was limited due to multiple scattering in the focal plane and the fact that the spectrometer was not designed for work on extended targets but for high resolution thin target experiments.

A fast trigger was provided by two layers of plastic scintillator. These were operated in coincidence to reduce random noise, and the output signals were combined in a mean-timing circuit to provide an accurate time fiducial.

The gas Čerenkov detector used isobutane at a pressure of 1 atm resulting in a detection threshold for electrons of about 10 MeV and for muons and pions of about 3 GeV. At the bottom of the gas Čerenkov detector were three paraboloidal mirrors which focused the Čerenkov light produced by passing charged particles onto three 12.7-cm-diam photomultiplier tubes. In addition to providing discrimination between electrons and heavier charged particles generated in the target, this detector also eliminated lower-energy cosmic ray muons.

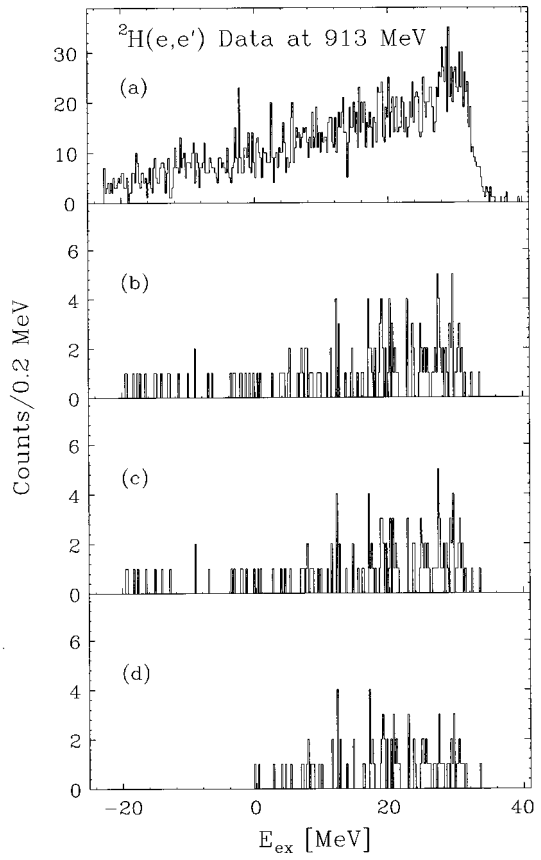

FIG. 5. The spectrum of scattered electrons from deuterium at the highest bombarding energy sorted on various detector cuts. In (a) the raw data spectrum is shown without using any cuts on the gas Čerenkov, focal plane, or lead-glass information. In (b), (c), and (d) cumulative cuts have been placed on the gas Čerenkov, focal plane, and lead-glass information, respectively.

The lead-glass Čerenkov detector consisted of a segmented array of 14 individual lead-glass blocks that were placed underneath the gas Čerenkov detector. These blocks were divided into a top and bottom layer of seven blocks each and were staggered to give complete coverage with a total thickness of 12 radiation lengths along the direction of the scattered electrons. The dimension of each block was 10×10 cm^2 at the face and 25 cm long. At one end of each block a photomultiplier tube was attached. The lead glass had a density of 5.18 g/cm^3, index of refraction 1.804, and a unit radiation length of 1.68 cm. This detector discriminated between electrons and the very high-energy cosmic ray muons (>3 GeV) that could trigger the gas Čerenkov detector since electrons generate a large electromagnetic shower, whereas the muons do not shower significantly.

The effectiveness of the various detector cuts that were used to reduce backgrounds is shown in Fig. 5 for the spectrum of scattered electrons from deuterium at the highest bombarding energy. In Fig. 5(a) the raw data spectrum is shown without using any cuts on the gas Čerenkov, focal plane, or lead-glass information. In Figs. 5(b), 5(c), and 5(d) cumulative cuts have been placed on the gas Čerenkov, focal plane, and lead-glass information, respectively, where the gas Čerenkov eliminates heavy charged particles (π^-'s), focal plane cuts eliminate cosmic rays, and the lead-glass cuts the remaining cosmic rays.

It can be seen when comparing Figs. 5(a) and 5(b) that the gas Čerenkov detector was effective at eliminating a large source of background. This background appeared to consist mostly of pions that originate from reactions initiated on the aluminum walls of the target section since pion production from deuterium is kinematically forbidden in this region. One such scenario is wide angle bremsstrahlung from the aluminum entrance end cap followed by the reaction ^{27}Al(γ,π^-) at 160° on the sides of the target cell which are not blocked by the collimating slits. Also pions directly from the reaction ^{27}Al(e^-,π^-) on the end caps can penetrate the collimating slits since the pions would be roughly minimum ionizing. These events did not restrict the analysis since they could be effectively eliminated by the gas Čerenkov detector.

The addition of focal plane and lead-glass detector cuts is shown in Figs. 5(c) and 5(d), respectively. It is easy to see from Fig. 5(d) that the reduction in cosmic ray background afforded by the lead-glass detector was crucial for understanding the data at this energy.

D. Data acquisition

The data stream from the various detectors was directed to a MicroVAX-based [34] acquisition system running the Los Alamos *Q* system [35,36]. A valid trigger consisted of a fast coincidence between the scintillator and either the gas Čerenkov detector or the lead-glass array. The delay line readout signals from each of the drift chambers were amplitude discriminated and sent to time-to-digital converters. The analog signals from the scintillators, gas Čerenkov detector, and lead-glass array were sent to analog-to-digital converters. For each trigger that was generated the information from all the detectors was written to magnetic tape for off-line analysis. Scaler readings and target logging were performed periodically during the course of the experiment and were also written to magnetic tape. A subset of the events was analyzed on line to allow identification and correction of problems that might occur during the experiment. Off-line replay of the data was by the same *Q* system used in the acquisition.

III. DATA ANALYSIS

The absolute differential threshold cross sections uncorrected for radiative effects is given by

$$\frac{d^2\sigma}{d\Omega dE_{np}}=\frac{N_{\rm scat}(E_{np})}{N_{\rm inc}n_{\rm tar}\langle\Omega z\rangle\varepsilon}, \tag{2}$$

where $N_{\rm scat}$ is the number of scattered electrons in the energy bin E_{np} corrected for the contribution from the ed elastic radiative tail, $N_{\rm inc}$ is the number of incident electrons, $n_{\rm tar}$ is the number of target centers per unit volume, $\langle\Omega z\rangle$ is the integrated solid angle, and ε is the electron detection efficiency. The integrated solid angle is given by the integral $\int\Omega(z)dz$ along the length of target and evaluated to be 13.5 ± 0.1 msr cm. The solid angle acceptance function $\Omega(z)$ was known very accurately by precise alignment of the target collimating slits and is shown in Fig. 6. The electron detection efficiency was independent of energy and determined to be (88 ± 1)% and the average liquid deuterium target density was 0.166 g/cm^3 with an uncertainty of one percent. Shown

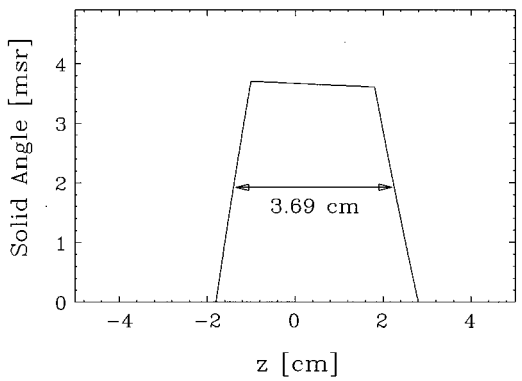

FIG. 6. The solid angle acceptance function defined by the ELSSY solid angle slits and the target collimating slits.

in Fig. 7 are the raw data spectra of scattered electrons for the deuteron electrodisintegration reaction. Except for the lowest bombarding energy these spectra represent the entire collected data set. As can be seen in the figure, the deuteron elastic peak at $E_{ex}=0$ was clearly visible for all but the highest bombarding energies.

The contribution from the *ed* elastic tail in the threshold region was extensively modeled, and this analysis is presented in Sec. III A. Two approaches have been taken to correct the inelastic threshold spectra for radiative effects. The first method described in Sec. III B used a radiative correction factor. This multiplicative factor corrected an energy bin for the fraction of events that have radiated out of the bin. The second method described in Sec. III C attempted a complete resolution unfolding of the measured spectra. This unfolding procedure yielded differential spectra that are experiment independent and can be compared directly with theoretical calculations.

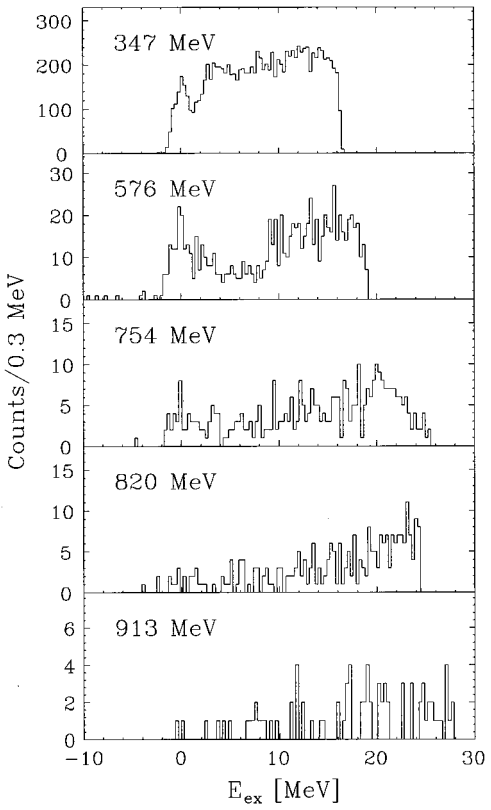

FIG. 7. The raw data spectra of scattered electrons from deuterium for the five bombarding energies used in this experiment. Except for the lowest bombarding energy these spectra are the entire collected data set.

The conversion of the threshold cross section differential in the scattered electron energy is given by

$$\frac{d^2\sigma}{d\Omega dE'}=\frac{dE_{np}}{dE'}\frac{d^2\sigma}{d\Omega dE_{np}}\simeq\eta\frac{d^2\sigma}{d\Omega dE_{np}}. \tag{3}$$

A. Elastic line shape

When an electron traverses matter it undergoes multiple interactions with the atoms of the medium that cause the electron to lose energy. The two major energy loss processes are collision losses, and the radiation of real photons either in the main scattering event (internal bremsstrahlung) or from other target nuclei (external bremsstrahlung). These energy loss processes shift and broaden the scattering peaks resulting in a line shape with a long tail toward lower momenta. The problem of calculating the elastic radiative line shape for small energy losses has been discussed by Bergstrom [37]. This calculation did not include radiative corrections from the nuclear current nor the effect of kinematic recoil. For the light targets (deuterium and hydrogen) that were used in this experiment these effects cannot be ignored. Tsai [38,39] calculated the radiative corrections for elastic scattering from hydrogen including these effects, and it is this result which was used in the present analysis to obtain the elastic line shape.

Following the method of Bergstrom [37], the elastic line shape was calculated for a general path through the target as a multiple convolution of the individual energy loss processes. A path through the target consisted of five pieces: (1) the target entrance foil, (2) the target liquid traversed before the scattering, (3) the scattering event including recoil, (4) the target liquid traversed after scattering, and (5) the target exit foil. The elastic line shape was given as a fivefold convolution of the energy losses over all these elements and an analytic solution was obtained. This expression, although similar to the Bergstrom result, has included the important effects of kinematic recoil and internal bremsstrahlung from the nuclear current. For our highest bombarding energy the latter effect was 5% for deuterium and 9% for hydrogen. The derivation of this result can be found in Ref. [32].

In the present experiment the analysis of the line shape was complicated by the fact that the spectrometer system had poor resolution of the target scattering vertex. Therefore, electrons accepted by the spectrometer could have traveled through a variety of different paths lengths in the target and each possible path represents a different line shape. The observed elastic line shape is thus given as a target average over all such paths. Integration over all possible paths, including multiple scattering effects, was not feasible to perform analytically and was carried out numerically by a Monte Carlo simulation. This was accomplished by first choosing randomly a possible path through the target and then picking an energy loss from the line shape distribution. The effect of multiple scattering was included, and each elec-

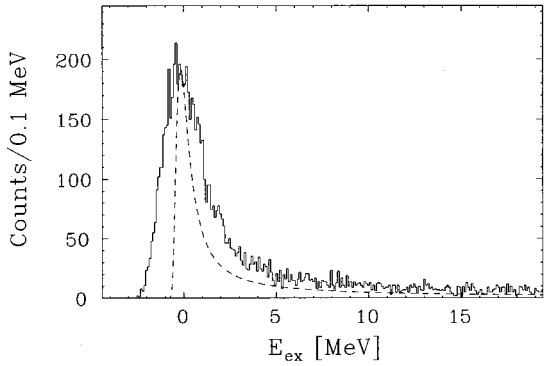

FIG. 8. Calculated experimental line shapes for electron-deuteron elastic scattering at 913 MeV and 160°. The histogram is the target-averaged line shape from the Monte Carlo calculation and the dashed curve is the line shape from the multiple convolution evaluated at the target center.

tron was followed until it emerged from the target where the final energy and coordinates were recorded.

Finally, the expected spectrum recorded by the detector system of the ELSSY spectrometer was calculated using the distribution of particle momentum and coordinates resulting from the Monte Carlo simulations. The trajectories of the particles through ELSSY and its detectors were calculated from the known optical matrix elements for this system [30]. These trajectories were then modified by multiple scattering in the detectors, and the coordinates at the detectors were broadened by their intrinsic spatial and angular resolutions.

A similar analysis was also performed [33] where the energy loss for each electron was calculated for each successive segment of path from the individual energy loss distributions. To account for internal bremsstrahlung the method of equivalent radiators was used but modified to also include the effect of radiation from the nuclear current [32]. The line shapes generated by either analysis agreed to within the statistical accuracy of the simulation.

Shown in Fig. 8 are calculations for the experimental line shapes for electron-deuteron elastic scattering at a bombarding energy of 913 MeV and scattering angle 160°. The histogram is the Monte Carlo calculation for the target-averaged line shape and the dashed curve is the line shape from the multiple convolution evaluated at the target center. This line shape was normalized to the peak of the Monte Carlo calculation. Both these line shapes have the characteristic long radiative tails and almost half of the events lie beyond 5 MeV of excitation. The target-averaged line shape is much broader due to the path length differences in the target. If the spectrometer system had allowed adequate reconstruction back to the target, corrections for the path length differences would have resulted with a narrower line shape more closely followed by the dashed curve.

In Fig. 9 the calculated line shapes are compared against measured data. For each spectrum the measured data are plotted as solid circles and the calculated line shapes as the histograms. The ordinate of each calculated line shape was arbitrarily normalized to the data at the peak since only the shape of the simulated spectrum is of consequence in the analysis. In Fig. 9(a) the comparison is shown for the spectrum of scattered electrons from ^{1}H at a bombarding energy of 913 MeV and angle 160° and in Fig. 9(b) for the spectrum

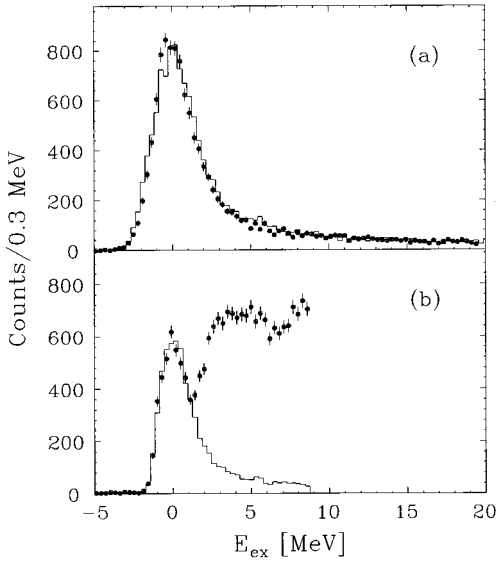

FIG. 9. Comparisons of the calculated and measured elastic line shapes for (a) electron-proton scattering at 913 MeV and 160° and (b) electron-deuteron scattering at 347 MeV and 160°. The measured data are plotted as the solid dots and the calculated line shapes as the histograms.

of scattered electrons from ^{2}H at a bombarding energy of 347 MeV and angle 160°. For the latter one sees both the elastic and inelastic scattering, and at the resolution of this experiment they are not totally separated. It is clear from this figure that the elastic line shapes were well understood and allowed an accurate description of the elastic radiative tail for subtraction from the inelastic region.

B. Radiative corrections

The absolute threshold cross section averaged over the range 0–Δ in E_{np} and corrected for radiative effects is given by

$$\left\langle \frac{d^2\sigma}{d\Omega dE_{np}} \right\rangle_{0-\Delta} = \frac{1}{\Delta} \frac{\int_0^{\Delta} N_{\rm scat}(E_{np})dE_{np}}{N_{\rm inc} n_{\rm tar} \langle \Omega z \rangle \varepsilon} \mathcal{R}^{0-\Delta}, \qquad (4)$$

where $\int_0^{\Delta} N_{\rm scat}(E_{np})dE_{np}$ is the number of inelastically scattered electrons contained in the interval 0–Δ, and $\mathcal{R}^{0-\Delta}$ is the radiative correction factor for that interval. For the purpose of comparing with existing data the averages from 0 to 3 and 0 to 10 MeV in E_{np} were chosen.

The radiative correction factor can be formally expressed as a ratio between the unradiated cross section, $\sigma(E_{np})$, to the radiated or measured cross section $\sigma^{\rm meas}(E_{np})$,

$$\mathcal{R}^{0-\Delta} = \frac{\int_0^{\Delta} \sigma(E_{np})dE_{np}}{\int_0^{\Delta} \sigma^{\rm meas}(E_{np})dE_{np}}. \qquad (5)$$

In order to obtain this correction the inelastic region was modeled as a continuous spectrum of elastic peaks. Then the elastic line shape analysis was used to describe the radiative effects for this region. The correction was divided into two factors:

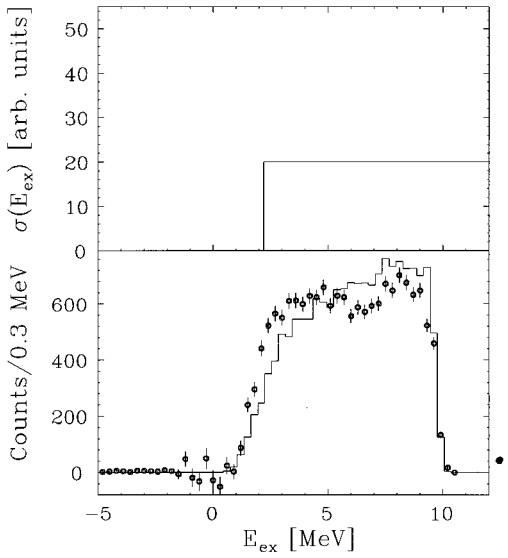

FIG. 10. Comparison of the Monte Carlo calculated and measured inelastic spectrum for deuteron breakup at 347 MeV. The measured data are plotted as solid circles and the Monte Carlo calculation as the histogram. The top panel is the assumed inelastic spectrum shape radiated by the Monte Carlo calculation.

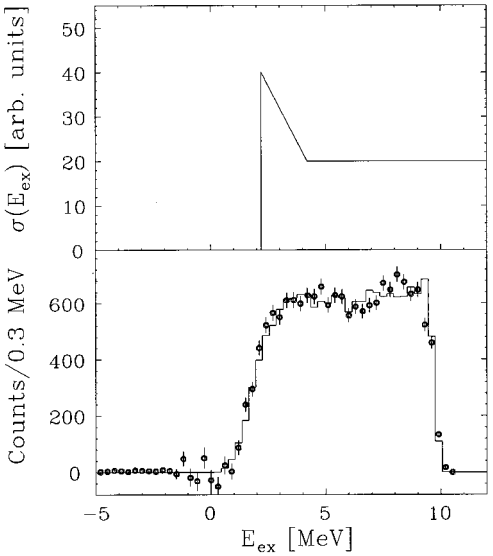

FIG. 11. Comparison of the Monte Carlo calculated and measured inelastic spectrum for deuteron breakup at 347 MeV. The measured data are plotted as solid circles and the Monte Carlo calculation as the histogram. The top panel is the assumed inelastic spectrum shape radiated by the Monte Carlo calculation.

$$\mathcal{R}^{0-\Delta}=e^{-\delta_2}\mathcal{F}^{0-\Delta}. \tag{6}$$

The first factor $e^{-\delta_2}$ was only a function of the scattering kinematics and corrected for the magnitude change in cross section due to the higher order scattering processes [32]. Typical values for this factor were of the order of 0.92 for all bombarding energies to within $\pm 1\%$. The second factor $\mathcal{F}^{0-\Delta}$ corrected for the fraction of events that have radiated out of the interval $0-\Delta$.

The Monte Carlo method that was used to evaluate the elastic line shape was also used to evaluate the correction factor $\mathcal{F}^{0-\Delta}$. This was accomplished by an iterative process. First, a reasonable shape for the unradiated inelastic threshold spectrum was chosen. This spectrum was then radiated using the energy losses modeled in the Monte Carlo calculation. The resultant radiated spectrum was then compared to the measured data. If they did not agree within statistics, the inelastic spectrum was modified and the process repeated until good agreement was achieved. From the unradiated and radiated spectrum the correction factor $\mathcal{F}^{0-\Delta}$ could be computed.

Unfortunately, this correction requires knowledge of the true threshold spectrum shape which is not known. Therefore, the resultant correction has an inherent model dependency which can be seen directly from Eq. (5). The correction depends on the detailed shape of the unradiated threshold spectrum. However, since it appears in both the numerator and denominator, the dependence is weak and can be tested directly for different spectrum shapes.

Figures 10 and 11 show a comparison of the calculated and measured deuteron breakup spectra for the lowest bombarding energy of 347 MeV. In each figure the top panel was the modeled inelastic breakup spectrum shape and the bottom panel compares its Monte Carlo radiated spectrum with the measured spectrum. The measured data with the elastic radiative tail subtracted are plotted as the solid circles and the calculated spectrum as the histogram. The calculated spectrum was also normalized to the total number of counts in the data. In Fig. 10 it is clear that a step function response for the inelastic spectrum that becomes nonzero at the breakup threshold does not reproduce the data very well. However, adding a resonancelike structure at the breakup energy yields a much better description of the data. This is not unreasonable and has been seen in existing measurements near this energy [11]. Using the results from Figs. 10 and 11 the extracted radiative correction factor $\mathcal{F}^{0-3}$ was 2.22 and 2.14, respectively. The finite difference illustrates the level of model dependency in the correction.

For the lower-energy data with good statistics the error in this correction was estimated to be no more than $\pm 2\%$. For the higher-energy data where the statistics were poorer the error in the correction was larger but estimated to be not more than $\pm 8\%$. However, statistical errors still dominate the cross section measurement uncertainties for the high-energy data points.

C. Radiative and resolution unfolding

In order to compare the measured threshold breakup spectra directly with theoretical predictions a complete radiative and resolution unfolding of the data was performed. The purpose of this was to obtain absolute spectra independent of experiment. For the unfolding, the inelastic region was modeled as a continuous spectrum of elastic peaks and the elastic line shape analysis was used to describe the radiative effects for this region. Then the observed spectrum of scattered electrons, σ^{meas}, is related to the true threshold spectrum σ by the convolution

$$\sigma^{\text{meas}}(E_{np})=e^{-\delta_2}\sigma^{R}(E_{np})=e^{-\delta_2}\int_{-\infty}^{\infty}\sigma(\varepsilon)R(E_{np}-\varepsilon)d\varepsilon, \tag{7}$$

where $R(x)$ is the experimental resolution function given by the elastic line shape and $e^{-\delta_2}$ corrected for the magnitude change in cross section due to the higher-order scattering processes [32]. In the following paragraphs the iterative method that was used to unfold the above equation is described. Since this was a delicate procedure, it is discussed in some detail.

The method of unfolding a spectrum was to find the true spectrum $\sigma(E_{np})$ which generated the observed spectrum $\sigma^R(E_{np})$ as given by Eq. (7). First, an initial guess was made for this distribution and labeled σ':

$$\sigma^{R'}(E_{np})=\int_{-\infty}^{\infty}\sigma'(\varepsilon)R(E_{np}-\varepsilon)d\varepsilon. \tag{8}$$

This expression can be manipulated into the form

$$\sigma^R(E_{np})=\int_{-\infty}^{\infty}\frac{\sigma^R(E_{np})}{\sigma^{R'}(E_{np})}\sigma'(\varepsilon)R(E_{np}-\varepsilon)d\varepsilon. \tag{9}$$

Since the resolution function $R(E_{np}-\varepsilon)$ is peaked at zero or $E_{np}=\varepsilon$, the following replacement can be made while introducing only a small error:

$$\sigma^R(E_{np})\simeq\int_{-\infty}^{\infty}\frac{\sigma^R(\varepsilon)}{\sigma^{R'}(\varepsilon)}\sigma'(\varepsilon)R(E_{np}-\varepsilon)d\varepsilon. \tag{10}$$

Therefore, the next guess for the true spectrum was given as

$$\sigma''(\varepsilon)=K(\varepsilon)\sigma'(\varepsilon), \tag{11}$$

where the correction factor $K(\varepsilon)$ is

$$K(\varepsilon)=\frac{\sigma^R(\varepsilon)}{\sigma^{R'}(\varepsilon)}. \tag{12}$$

This procedure was repeated until the folded spectrum $\sigma^{R'\cdots}$ became statistically equivalent to the measured spectrum σ^R. When this was satisfied the result for the resolution unfolded spectrum was given by $\sigma'^{\cdots}$.

The unfolding procedure, although mathematically well defined and unique, was problematic since the spectrum shapes were not known exactly but only statistically as presented in the data. Therefore, during the unfolding process, the statistical scatter in the original spectrum was magnified at each iteration when the next guess was calculated. This leads to unfolded results with unreasonably large amounts of jitter in the data points. These solutions are allowed and originate from the following ambiguity: Any function $\mathcal{N}$ which when added to the unfolded result σ' and then folded again with the resolution function whose effect does not statistically change the result is also a statistically acceptable solution. A class of such functions which satisfies this criterion are periodic functions. The space of these functions is related to the width of the resolution function; the broader the resolution width, the larger the period for these functions can become. The resolution widths in this experiment were of the order of 2 MeV FWHM. Therefore, when unfolding the threshold spectrum with bin widths less than 2 MeV many statistically acceptable solutions existed. However, the addition of these solutions made the unfolded result appear excessively jittery. Since the shape of the threshold spectrum was expected to be a smoothly varying function such solutions were rejected on physical grounds. During the unfolding procedure these solutions were suppressed at each iteration with the following modifications [40,32].

The correction factors $K(\varepsilon_i)$, where i labels the energy bin, were smoothed [41] since the ratio is expected to be a smoothly varying function. Then the smoothed correction factors were only applied to those energy bins where the difference between the measured and folded spectrum was considered statistically significant. An application of Chauvenet's criterion [42] was used to quantify that statement. For a given energy bin the number of standard deviations, $z(\varepsilon_i)$, by which the folded spectrum differed from the measured spectrum was calculated:

$$z_i=\left|\frac{\sigma^R(\varepsilon_i)-\sigma^{R'}(\varepsilon_i)}{\delta\sigma^R(\varepsilon_i)}\right|. \tag{13}$$

Based on a normal distribution one expects to see $[1-\mathrm{erf}(z_i/\sqrt{2})]N$ data points to be z_i or more away where N is the total number of data points in the spectrum. If this amount is less than one-half the number actually observed, then it is considered to be statistically significant. Mathematically, this is expressed as

$$[1-\mathrm{erf}(z_i/\sqrt{2})]N<\frac{1}{2}\sum_{j=1}^{N}u(z_j-z_i), \tag{14}$$

where $u(z)$ is the unit step function with $u(0)=1$. Solving for z_i yielded the statistical criterion for the difference between the measured and folded spectrum in the ith bin to be significant:

$$z_i>\sqrt{2}\,\mathrm{erf}^{-1}\left\{1-\frac{1}{2N}\sum_{j=1}^{N}u(z_j-z_i)\right\}. \tag{15}$$

For the initial guess a step function distribution was chosen which became nonzero at the breakup threshold. This ensured that the following iterative guesses would also start at the breakup threshold. This is appropriate since the true inelastic spectrum is expected to start at the breakup threshold. The iterative procedure was stopped when the number of bins that were considered statistically significant was either zero or did not change from the previous iteration. In all cases no more than four iterations were needed with reduced χ^2 of the order of one.

Figure 12 illustrates the effect of including the smoothing and statistical criterion in the unfolding procedure for the deuteron electrodisintegration data at 347 MeV. In Fig. 12(a) the unfolded spectrum is shown without using these additions. This was stopped after three iterations when χ_r^2 dropped below 1. This spectrum appears unacceptably jittery. Figure 12(b) is the result generated using the modifications and was accepted as the final result.

This procedure was used to unfold all the electrodisintegration data except at the highest bombarding energy where

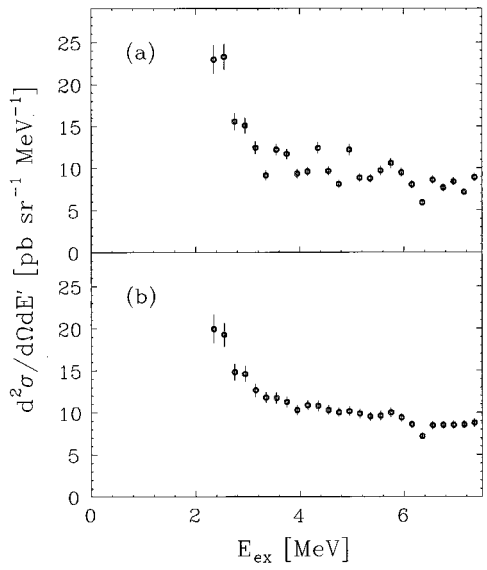

FIG. 12. Unfolded spectra for the deuteron electrodisintegration data at 347 MeV. In (a) the spectrum was generated without using the smoothing and statistical criterion discussed in the text, and in (b) both of these were added to the unfolding procedure.

it was limited due to extremely poor statistics. Computed average cross sections were also consistent with the analysis of Sec. III B.

D. Backgrounds

Possible sources of background can be grouped into two categories: those associated with the electron beam on target and those independent of it. Background from beam independent sources, primarily energetic cosmic ray muons, was kept at a minimum by using stringent focal plane acceptance cuts. By performing measurements without the electron beam it was determined that background from this source was negligible. Background associated with beam on target is more difficult to discriminate since it originates at the target and therefore within the acceptance cuts. Target collimating slits were used to block the contribution from electron scattering from the aluminum endcaps of the target cell. However, exotic processes such as $\gamma d \rightarrow \pi^0 d$, $\pi^0 \rightarrow \gamma\gamma$, $\gamma \rightarrow e^+e^-$, $\gamma d \rightarrow \gamma d$, and $\gamma \rightarrow e^+e^-$ can contribute electrons into the acceptance. These sources were estimated to be much smaller than the measured cross sections and neglected in the analysis.

E. Systematic uncertainties

The largest source of systematic uncertainty in extracting the breakup cross sections was associated with the accuracy with which the elastic peak position could be located (see Fig. 7). An uncertainty in this position affects the correct location of the threshold breakup region. For the lower-energy measurements where well-defined elastic peaks existed this represented a relatively small uncertainty. At higher energies where the statistics were poorer and a well-defined elastic peak did not exist, this yielded a proportionally larger uncertainty in the cross sections. At 820 MeV this uncertainty was estimated to be of the order of $\pm 30\%$. However, at the highest bombarding energy, 913 MeV, elastic scattering data from hydrogen were also measured, and this allowed an accurate calibration for the deuterium elastic peak position, yielding a relatively smaller uncertainty at that energy. The estimated systematic uncertainties in the elastic peak positions and the overall estimated systematic uncertainties associated with each measurement are presented in Table I. These overall uncertainties are smaller than the statistical errors except at the lowest bombarding energy.

TABLE I. Estimated systematic uncertainties.

E [MeV]	E_{ex}^{el} [MeV]	$\langle d^2\sigma/d\Omega dE' \rangle_{0-3}$	$\langle d^2\sigma/d\Omega dE' \rangle_{0-10}$
347	± 0.05	$\pm 4\%$	
576	± 0.15	$\pm 9\%$	
754	± 1.0	$\pm 14\%$	$\pm 4\%$
820	± 2.0	$\pm 30\%$	$\pm 10\%$
913	± 1.5	$\pm 20\%$	$\pm 8\%$

IV. RESULTS AND COMPARISONS

New measurements for the electrodisintegration of the deuteron near the breakup threshold are presented in Table II as cross sections averaged over E_{np} from 0 to 3 and from 0 to 10 MeV. The uncertainties quoted in the table are only statistical. The systematic uncertainties are given in Table I.

In Fig. 13 the new cross section measurements averaged from 0 to 3 MeV are included with previous data for this reaction. These new data are represented in the figure as the solid circles. The measurements performed at Saclay also averaged from 0 to 3 MeV are represented by the open squares and the SLAC measurements averaged from 0 to 10 MeV as the open diamonds. As can be seen in the figure, the agreement between the three data sets in the region of overlap is good. The two lowest new Q^2 data points agree quite well with the Saclay measurements averaged over a similar interval. The three highest new Q^2 data points also agree well with the SLAC measurements that were averaged from 0 to 10 MeV. The most dramatic feature of the combined Saclay and SLAC data sets is the sharp departure from a purely exponential slope at $Q^2 \approx 27$ fm^{-2}. This transition occurs at the adjoining region between these two data sets. The new measurements have coverage throughout this region and also support this dependence.

In this figure these data are also compared to a nonrela-

TABLE II. New experimental data for deuteron electrodisintegration near threshold at 160°. The results are laboratory cross sections averaged over the relative energy of separation, E_{np}, of the recoiling np system from 0 to 3 MeV and from 0 to 10 MeV. The errors quoted included only statistical uncertainties.

E [MeV]	Q^2 [fm^{-2}]	$\langle d^2\sigma/d\Omega dE' \rangle_{0-3}$ [μb sr^{-1} MeV^{-1}]	$\langle d^2\sigma/d\Omega dE' \rangle_{0-10}$ [μb sr^{-1} MeV^{-1}]
347	8.66	$1.20 \pm 0.02 \times 10^{-5}$	
576	20.5	$4.39 \pm 0.66 \times 10^{-8}$	
754	31.6	$4.09 \pm 1.05 \times 10^{-9}$	$5.47 \pm 0.60 \times 10^{-9}$
820	36.0	$1.64 \pm 0.53 \times 10^{-9}$	$2.56 \pm 0.41 \times 10^{-9}$
913	42.4	$1.89 \pm 0.75 \times 10^{-9}$	$1.87 \pm 0.39 \times 10^{-9}$

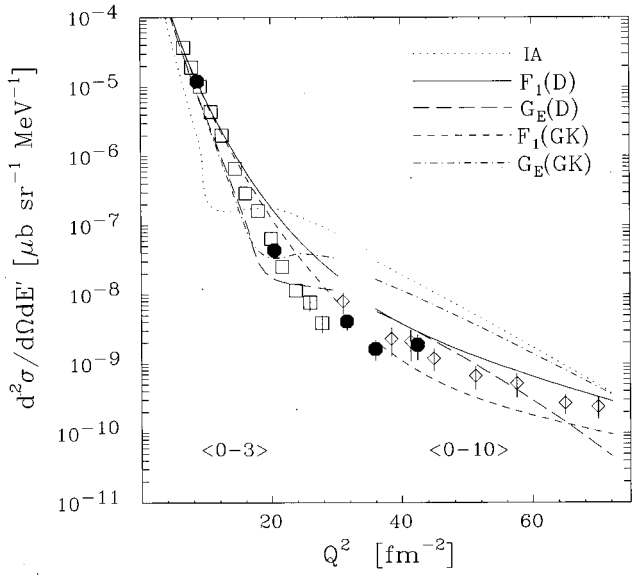

FIG. 13. Calculations for backward threshold electrodisintegration of the deuteron using the Argonne v_{14} potential [19] compared with experimental data. The dotted curve is the result for the impulse approximation calculation (IA). The solid curve is the meson exchange current (MEC) calculation using the Dirac F_1 form factor with the dipole (D) parametrization for the nucleon electromagnetic form factors ($G_{En}\neq 0$) [43]. The long dashed curve is the same calculation using instead the Sachs G_E form factor. The short dashed and dot-dashed curves are the corresponding results with the Gari and Krümpelmann (GK) parametrization for the nucleon electromagnetic form factors [44]. The new measurements averaged from 0 to 3 MeV are represented by the solid circles, the Saclay data averaged from 0 to 3 MeV as the open squares, and the SLAC data averaged from 0 to 10 MeV as the open diamonds.

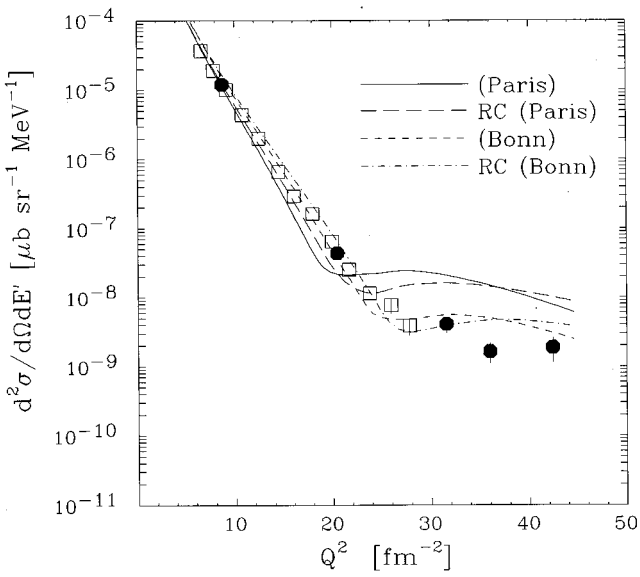

FIG. 14. Paris and Bonn potential calculations for deuteron electrodisintegration including lowest-order relativistic corrections. Calculations were evaluated at $E_{np}=1.5$ MeV and for a laboratory electron scattering angle of 155° [45]. The solid curve is the Paris potential calculation including meson exchange currents (MEC's) and isobar configurations (IC's) using the Sachs G_E form factor and the dipole nucleon electromagnetic form factors ($G_{En}\neq 0$) [43]. The long dashed curve is the same calculation including lowest-order relativistic contributions (RC's) to the current operator and kinematic wave function boost. The short dashed and dot-dashed curves are the corresponding results with the Bonn potential.

tivistic calculation for deuteron electrodisintegration by Schiavilla and Riska [19]. These calculations are for the Argonne v_{14} potential and includes partial waves up to $J\leqslant 2$ in the final scattering state. The results of the calculations have been averaged over E_{np} from 0 to 3 MeV and from 0 to 10 MeV to correspond to the data, and the break in the curves separates the two averages. Shown in the figure is the impulse approximation (IA) calculation along with meson exchange current (MEC) calculations that illustrate the sensitivity to the choice of form factor F_1 or G_E, as well as the parametrization of the nucleon electromagnetic form factors, dipole (D) with $G_{En}\neq 0$ [43] or Gari and Krümpelmann (GK) [44]. As can be seen all these calculations show the necessity for MEC to reproduce the data in the region near the IA diffraction minimum, $Q^2\approx 12$ fm^{-2}. For $Q^2 > 20$ fm^{-2} wide variations exist in the predictions mostly due to the choice of form factor F_1 or G_E. In a nonrelativistic framework the correct choice of form factor is ambiguous and the fact that the predictions differ between F_1 and G_E indicates that relativistic corrections are significant. The difference due to the nucleon electromagnetic form factor parametrization, which comes mostly from the neutron electric form factor, is seen to be not as large. These calculations do seem to predict a change in slope which is seen in the data at $Q^2\approx 27$ fm^{-2}. However, for the F_1 calculation the change is too gradual and for G_E it is located at a smaller Q^2.

In Fig. 14 a calculation of Wilbois, Beck, and Arenhövel [45] is shown that includes some lowest-order relativistic corrections (RC's). These calculations were performed for the Paris and Bonn potentials including MEC and isobar configurations using the Sachs G_E form factor and the dipole parametrization for the nucleon electromagnetic form factors ($G_{En}\neq 0$) [43]. These calculations were performed both with and without the lowest-order RC and were evaluated at $E_{np}=1.5$ MeV. From the figure it can be seen that the dependence of the potential model on the results is as large as the RC. The effect of the RC for both potential models is to increase the strength of the cross section for $Q^2<20$ fm^{-2}, improving the description of the data.

In Fig. 15 the calculations of Wilbois *et al.* [45] are compared with the radiative and resolution unfolded spectra. As can be seen, none of the calculations can describe the data at all four energies equally well; however, the overall shapes of the breakup continuum are reasonably reproduced. These data provide clear evidence for a resonance peak at the breakup threshold at the two lowest energies and a slight enhancement is seen at 754 MeV. The data at 820 MeV show no evidence is for such a structure. All calculations describe a resonance peak at threshold except at 576 MeV.

Shown in Fig. 16 is another relativistic calculation by Smejkal, Truhlík, and Göller [46]. In their model a chiral Lagrangian of the $N\pi\rho a_1$ system is constructed within the framework of the hidden local symmetries (HLS's) approach. From this Lagrangian the isovector electromagnetic current operators are constructed and applied to the electrodisintegration of the deuteron. The exchange currents include

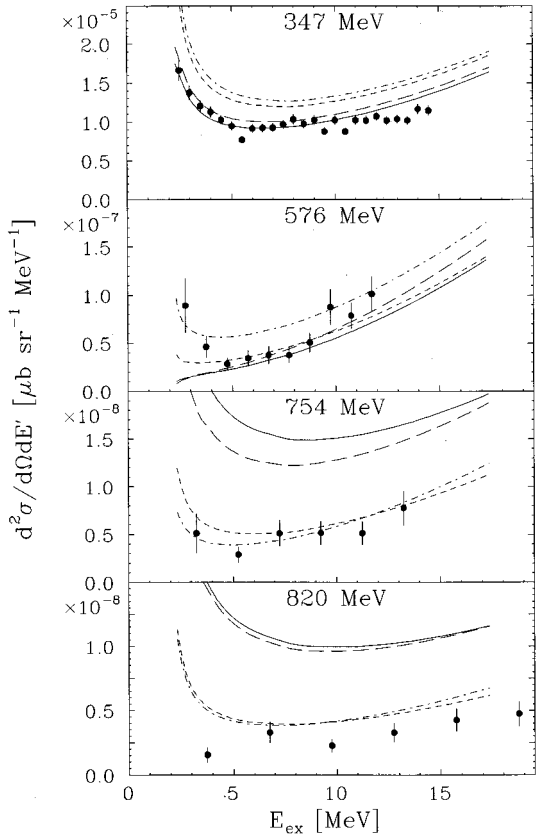

FIG. 15. Differential spectra for deuteron electrodisintegration compared with the new measurements represented as solid circles. The calculations are for both the Paris and Bonn potentials at $\theta_e^{\rm lab} = 160°$ with and without lowest-order relativistic corrections [45]. These calculations are the same as those presented in Fig. 14. The solid curve is the Paris potential calculation including meson exchange currents (MEC's) and isobar configurations (IC's) using the Sachs G_E form factor and the dipole nucleon electromagnetic form factors ($G_{En} \neq 0$) [43]. The long dashed curve is the same calculation including lowest order relativistic contributions (RC's) to the current operator and kinematic wave function boost. The short dashed and dot-dashed curves are the corresponding results with the Bonn potential.

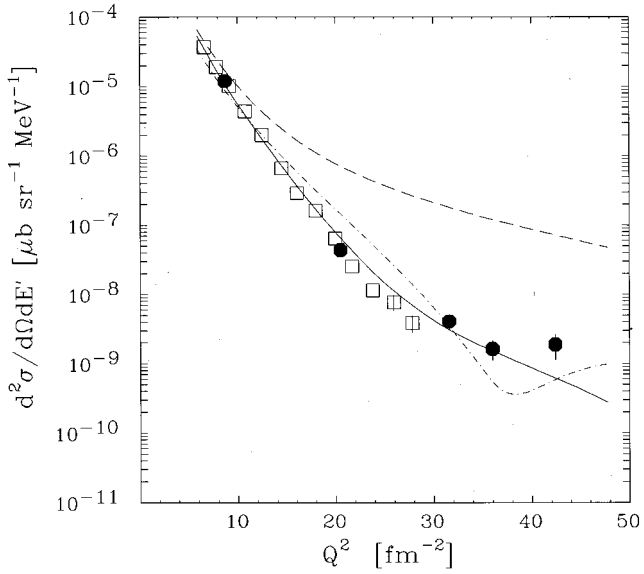

FIG. 16. A relativistic meson exchange calculation [46] and a hybrid quark-hadron model calculation [48] for deuteron electrodisintegration near threshold. The solid curve is the relativistic meson exchange calculation with the Bonn OBEPQB potential modified to include a_1 exchange. The dashed curve is a similar calculation to the solid curve except with the a_1 meson eliminated in the correct chiral model. The dot-dashed curve is a hybrid quark-hadron model calculation.

the standard $\pi+\rho$ MEC's as well as the a_1-π exchange current. The one-body current and π MEC include a full set of leading order relativistic corrections. The calculations are for the Bonn OBEPQB potential [47] modified to include a_1 meson exchange. The cross sections are evaluated at $E_{np} = 1.5$ MeV, electron scattering angle of 160°, and include partial waves up to $L \leqslant 3$. The solid curve shown in the figure is the result with the Höhler H7.1 parametrization for the nucleon electromagnetic form factors [48]. This calculation describes the trend of the data up to $Q^2 \approx 36$ fm^{-2}. The dashed curve is a similar calculation to the solid curve except with the a_1 meson eliminated in the correct chiral model. This calculation does not describe the data even at relatively low Q^2 showing the importance of the a_1 meson degrees of freedom in the Lagrangian.

Also shown in Fig. 16 as the dot-dashed curve is a hybrid quark-hadron calculation by Lu and Cheng [49] based on the Kisslinger model. This model attempts to match the long and medium range meson exchange potentials with six-quark cluster potentials at short distances by describing the np system in two distinct sectors: a two-baryon exterior region ($r \geqslant r_0$) and a six-quark cluster interior region ($r < r_0$) where r_0 is the matching radius. For the calculation presented in the figure a matching radius of 0.8 fm was chosen and the cross sections were evaluated at $E_{np} = 1.5$ MeV with an electron scattering angle of 160°. As can be seen in the figure this calculation can qualitatively describe the trend of the data. However, a result of this model is the presence of a small second maximum in the cross section just above 50 fm^{-2}. It is speculated that this second maximum might be the signature for six-quark cluster formation in the deuteron. The new measurements presented in this paper have coverage in this region with good resolution and do not show this feature.

V. CONCLUSIONS

In this paper new measurements for the threshold electrodisintegration of the deuteron are reported. These measurements were made with good resolution and cover a Q^2 region between 8 and 42 fm^{-2}. In the region of overlap these new measurements agree with a previous good resolution experiment at Saclay [11] and a poorer resolution experiment at SLAC [25]. These new data also support the observed departure of the cross section from a purely exponential slope at $Q^2 \approx 27$ fm^{-2}. No evidence for a second maximum in the cross section is seen above $Q^2 \approx 27$ fm^{-2}. Comparisons of the data are made with several types of calculations: nonrelativistic, nonrelativistic including lowest-order relativistic corrections, and a hybrid quark-hadron model. All calculations show the necessity of meson exchange currents to explain the absence of the deep diffraction minimum at

$12\ \mathrm{fm}^{-2}$ produced by the one-body amplitudes. However, none of the calculations can completely describe the data over the entire measured Q^2 range. The dependence of the calculations on the potential model or nucleon electromagnetic form factors is large, and the lowest-order effects of relativity are seen to be just as large even at intermediate Q^2. It has become clear that further advancement in the interpretation of this reaction will require better knowledge of the nucleon electromagnetic form factors as well as relativistic corrections. Comparison with a hybrid quark-hadron model shows no compelling evidence for the breakdown of the conventional meson-nucleon theories requiring explicit inclusion of the underlying quark structure.

ACKNOWLEDGMENTS

We would like to acknowledge the efforts of the MIT-Bates staff, especially K. Dow and J. Dzengeleski, for their technical support during the experiment. We also would like to thank H. Arenhövel for providing his calculations and L.C. Lu and E. Truhlík for providing their calculations prior to publication. This work was supported by the U.S. Department of Energy Grant No. DE-FG02-ER40415 and Contract Nos. DE-AC02-ER03069 and DE-FG02-94ER40818, and by National Science Foundation Grant No. 87-15050. A.H. acknowledges the support of the Monbusho International Research Program and the Saito Science Foundation.

[1] G. A. Peterson and W. C. Barber, in *Proceedings of the Rutherford Jubilee International Conference*, edited by J. B. Birks (Academic Press, New York, 1961), p. 831; H. W. Kendall, J. I. Friedman, E. F. Erickson, and P. A. M. Gram, Phys. Rev. **124**, 1596 (1961); G. A. Peterson and W. C. Barber, *ibid.* **128**, 812 (1962); M. R. Yearian and E. B. Hughes, Phys. Lett. **10**, 234 (1964); J. Goldemberg and C. Schaerf, *ibid.* **20**, 193 (1966); R. E. Rand, R. F. Frosch, C. E. Littig, and M. R. Yearian, Phys. Rev. Lett. **18**, 469 (1967).

[2] D. Ganichot, B. Grossetête, and D. B. Isabelle, Nucl. Phys. **A178**, 545 (1972).

[3] L. Katz, G. Ricco, T. E. Drake, and H. S. Caplan, Phys. Lett. **28B**, 114 (1968); G. Ricco, T. E. Drake, L. Katz, and H. S. Caplan, Phys. Rev. C **1**, 391 (1970).

[4] G. G. Simon, F. Borkowski, Ch. Schmitt, V. H. Walther, H. Arenhövel, and W. Fabian, Phys. Rev. Lett. **37**, 739 (1976); G. G. Simon, F. Borkowski, Ch. Schmitt, V. H. Walther, H. Arenhövel, and W. Fabian, Nucl. Phys. **A324**, 277 (1979).

[5] V. Z. Jankus, Phys. Rev. **102**, 1586 (1956).

[6] J. Hockert, D. O. Riska, M. Gari, and A. Huffman, Nucl. Phys. **A217**, 14 (1973).

[7] J. A. Lock and L. L. Foldy, Ann. Phys. (N.Y.) **93**, 276 (1975).

[8] W. Fabian and H. Arenhövel, Nucl. Phys. **A258**, 461 (1976).

[9] B. Sommer, Nucl. Phys. **A308**, 263 (1978).

[10] M. Bernheim *et al.*, Phys. Rev. Lett. **46**, 402 (1981).

[11] S. Auffret *et al.*, Phys. Rev. Lett. **55**, 1362 (1985).

[12] W. Leidemann and H. Arenhövel, Nucl. Phys. **A393**, 385 (1983).

[13] J. F. Mathiot, Nucl. Phys. **A412**, 201 (1984).

[14] A. Buchmann, W. Leidemann, and H. Arenhövel, Nucl. Phys. **A443**, 726 (1985).

[15] S. K. Singh, W. Leidemann, and H. Arenhövel, Z. Phys. A **331**, 509 (1988); and (private communication).

[16] E. Truhlík and J. Adam, Jr., Nucl. Phys. **A492**, 529 (1989).

[17] R. Dymarz and F. C. Khanna, Phys. Rev. C **41**, 828 (1990).

[18] W. Leidemann, K.-M. Schmitt, and H. Arenhövel, Phys. Rev. C **42**, R826 (1990).

[19] R. Schiavilla and D. O. Riska, Phys. Rev. C **43**, 437 (1991); and (private communication).

[20] Y. Yamauchi, R. Yamamoto, and M. Wakamatsu, Nucl. Phys. **A443**, 628 (1985).

[21] T. S. Cheng and L. S. Kisslinger, Nucl. Phys. **A457**, 602 (1986).

[22] Y. Yamauchi, A. Buchmann, and A. Faessler, Nucl. Phys. **A494**, 401 (1989).

[23] K. S. Lee *et al.*, Phys. Rev. Lett. **67**, 2634 (1990).

[24] R. G. Arnold *et al.*, Phys. Rev. C **42**, R1 (1990).

[25] M. Frodyma *et al.*, Phys. Rev. C **47**, 1599 (1993).

[26] D. Beck, Ph.D. thesis, Massachusetts Institute of Technology, 1986.

[27] P. C. Dunn, Nucl. Instrum. Methods **165**, 163 (1979).

[28] C. F. Williamson, Bates LINAC Internal Report No. 88-01, 1988.

[29] W. M. Schmitt and C. F. Williamson, Bates LINAC Internal Report No. 90-02, 1990.

[30] W. Bertozzi, M. V. Hynes, C. P. Sargent, W. Turchinetz, and C. Williamson, Nucl. Instrum. Methods **162**, 211 (1979).

[31] W. Bertozzi *et al.*, Nucl. Instrum. Methods **141**, 457 (1977).

[32] W. M. Schmitt, Ph.D. thesis, Massachusetts Institute of Technology, 1993.

[33] K. S. Lee, Ph.D. thesis, University of Massachusetts, Amherst, 1993.

[34] MicroVAX is a trademark of Digital Equipment Corporation.

[35] LAMPF Internal Report No. MP-1-3401-3, 1985.

[36] LAMPF Internal Report No. MP-1-3414-2, 1986.

[37] J. Bergstrom, MIT 1967 Summer Study: Medium Energy Nuclear Physics with Electron Linear Accelerators, 1967, p. 251.

[38] Y. S. Tsai, Phys. Rev. **122**, 1898 (1961).

[39] L. Mo and Y. S. Tsai, Rev. Mod. Phys. **41**, 205 (1969).

[40] D. Potterveld, Ph.D. thesis, California Institute of Technology, 1989.

[41] P. Bevington, *Data Reduction and Error Analysis in the Physical Sciences* (McGraw-Hill, New York, 1969).

[42] H. Young, *Statistical Treatment of Experimental Data* (McGraw-Hill, New York, 1962).

[43] S. Galster *et al.*, Nucl. Phys. **B32**, 221 (1971).

[44] M. Gari and W. Krümpelmann, Phys. Lett. B **173**, 10 (1986).

[45] T. Wilbois, G. Beck, and H. Arenhövel, Few-Body Syst. **15**, 39 (1993); (private communication).

[46] J. Smejkal, E. Truhlík, and H. Göller, Nucl. Phys. A (submitted); (private communication).

[47] E. Truhlík and K.-M. Schmitt, Few-Body Syst. **11**, 155 (1992).

[48] G. Höhler *et al.*, Nucl. Phys. **B114**, 505 (1976).

[49] L. C. Lu and T. S. Cheng, Phys. Lett. B **386**, 69 (1996).